# The Interaction of Recirculation Gyres and a Deep Boundary Current

ISABELA ASTIZ LE BRAS

*Scripps Institution of Oceanography, University of California, San Diego, La Jolla, California, and Massachusetts Institute of Technology–Woods Hole Oceanographic Institution Joint Program in Physical Oceanography, Woods Hole, Massachusetts*

STEVEN R. JAYNE AND JOHN M. TOOLE

*Woods Hole Oceanographic Institution, Woods Hole, Massachusetts*

(Manuscript received 3 October 2017, in final form 10 January 2018)

ABSTRACT

Motivated by the proximity of the Northern Recirculation Gyre and the deep western boundary current in the North Atlantic, an idealized model is used to investigate how recirculation gyres and a deep flow along a topographic slope interact. In this two-layer quasigeostrophic model, an unstable jet imposed in the upper layer generates barotropic recirculation gyres. These are maintained by an eddy-mean balance of potential vorticity (PV) in steady state. The authors show that the topographic slope can constrain the northern recirculation gyre meridionally and that the gyre's adjustment to the slope leads to increased eddy PV fluxes at the base of the slope. When a deep current is present along the topographic slope in the lower layer, these eddy PV fluxes stir the deep current and recirculation gyre waters. Increased proximity to the slope dampens the eddy growth rate within the unstable jet, altering the geometry of recirculation gyre forcing and leading to a decrease in overall eddy PV fluxes. These mechanisms may shape the circulation in the western North Atlantic, with potential feedbacks on the climate system.

## 1. Introduction

In the western North Atlantic, the Gulf Stream carries warm, salty water of tropical and subtropical origin toward the high latitudes, while the deep-reaching deep western boundary current (DWBC) brings cold, fresh water of high-latitude origin equatorward. The combined effect of these two currents is a poleward heat transport in the North Atlantic, aiding in the stabilization of Earth's climate (Wunsch 2005). The Gulf Stream and DWBC come in close contact at Cape Hatteras, where the DWBC is forced under the Gulf Stream (Pickart and Smethie 1993), and at the Tail of the Grand Banks, where the currents are adjacent (Mertens et al. 2014). The interaction between the Gulf Stream and DWBC at these two locations has been the focus of previous work (e.g., Hogg and Stommel 1985; Spall 1996; Gary et al. 2011; Buckley and Marshall 2015).

Between Cape Hatteras and the Tail of the Grand Banks, the Gulf Stream has a cyclonic recirculation cell to its north: the Northern Recirculation Gyre (NRG). The barotropic NRG coexists with the DWBC at depth (Worthington 1976; Hogg 1983; Richardson 1985), and there is evidence of exchange between them from tracer observations (Hogg et al. 1986; Pickart et al. 1989) and acoustically tracked floats (Bower et al. 2009, 2011). High-resolution models reproduce this exchange and indicate a southward interior pathway for water of subpolar origin within the Gulf Stream's recirculation gyres (Gary et al. 2011; Lozier et al. 2013). These models show a continuous distribution of synthetic floats from the slope to the offshore edge of the recirculation gyres, indicating exchange between the DWBC and the NRG. In this study, we model the interaction between the NRG and the DWBC in an idealized framework. This interaction is of fundamental interest because of its potential feedbacks on the structure of the horizontal and overturning circulations in the western North Atlantic and their associated poleward heat transport.

Large-scale ocean dynamics are often cast in terms of potential vorticity (PV), a dynamical tracer that is conserved barring forcing or dissipation. In a steady-state balance of PV, eddy motions on relatively short time scales can drive flows across time-mean PV contours

*Corresponding author*: Isabela Astiz Le Bras, ilebras@ucsd.edu

DOI: 10.1175/JPO-D-17-0206.1

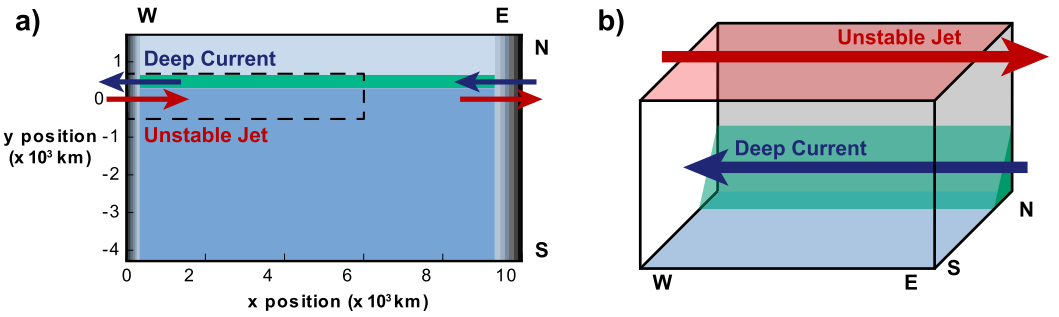


FIG. 1. (a) Plan view of the full model domain. The dashed box highlights the portion of the domain that is the focus of our analysis. Gray shading on the east and west represent the sponge regions, in which friction increases linearly toward the boundaries. The green band indicates the location of the topographic slope in the lower layer. The lower layer is shallower to the north of the topographic slope. (b) The unstable jet (red) is in the model upper layer, and the deep current (dark blue) flows along the topography in the lower layer, as depicted schematically.

(Holland and Rhines 1980). Rhines and Holland (1979) explained that eddies tend to flux PV downgradient, and Rhines and Young (1982) further showed that eddies homogenize PV within closed circulation contours. Through connections to these theoretical developments, Hogg (1983) proposed that the NRG and its anticyclonic counterpart to the south of the Gulf Stream are driven by Gulf Stream eddies.

The theory of recirculation gyres developed in several directions. Fofonoff (1954) had shown that inertial gyres can emerge from the mean advection of PV along streamlines. This idea was developed further, including stratification in Marshall and Nurser (1986), Greatbatch (1987), and Cessi (1990). Another body of work included the effects of relative vorticity and used localized vorticity forcing to mimic eddies (Haidvogel and Rhines 1983; Cessi et al. 1987; Cessi 1988; Malanotte-Rizzoli et al. 1995; Berloff et al. 2007; Waterman and Jayne 2012). The focus of this work was on the generation of rectified flows from eddy-mean and eddy–eddy interaction, and on isolating the effect of eddies in forcing recirculation gyres.

A related class of previous work used unstable jets to generate eddies, including both eddy forcing and inertial time-mean advection of PV along streamlines (Jayne et al. 1996; Beliakova 1999; Jayne and Hogg 1999; Mizuta 2009). In this framework, eddies generated by an unstable jet act to smooth PV, creating homogeneous regions within which inertial recirculations can develop. Waterman and Jayne (2011) studied this phenomenon in a two-layer quasigeostrophic (QG) model, describing the along-stream development of eddy roles and highlighting that downstream enstrophy convergence results in upgradient PV fluxes that drive recirculation gyres.

Here, we extend the model of Waterman and Jayne (2011) to include a zonal continental slope to the north of the recirculation gyres, as well as a deep current on the slope (Fig. 1). While we mimic the configuration in the North Atlantic, our objective is to use this idealized setup to gain dynamical insights that are generalizable to other oceanic settings in which eddy-driven flows encounter topographic slopes. Our model setup is described in section 2. In section 3, we highlight our results: the effects of the topographic slope and deep current on recirculation gyre dynamics as well as the consequences for the deep current. We discuss the implications of this study in section 4.

## 2. Model setup

Our model is based on the quasigeostrophic setup introduced in Jayne et al. (1996) to study the dynamics of recirculation gyres and extended to two layers by Waterman and Jayne (2011). The model is set in a channel with zonal flow prescribed at the eastern and western boundaries and solid boundaries to the north and south. An unstable jet flows from west to east in the upper layer, and a deep current flows in the opposite direction in the lower layer, offset to its north, along a zonal continental slope (Fig. 1).

The governing equations for this two-layer quasigeostrophic model are the conservation equations for nondimensional quasigeostrophic PV $q_n$, which is given by

$$q_n = \nabla^2\psi_n + \beta y + (-1)^n \frac{1}{S_n}(\psi_1 - \psi_2) + \eta_B(n-1). \qquad (1)$$

The subscript $n$ denotes the layer, that is, $n = 1$ corresponds to the upper, surface layer and $n = 2$ to the lower, deep layer. The variable $\psi_n$ is the nondimensional streamfunction in the $n$th layer. The PV in each layer is the sum of the relative vorticity in the layer, $\zeta_n = \nabla^2\psi_n$; the planetary vorticity $\beta y$, where $\beta$ is a constant approximation to the slope of the Coriolis parameter $f$;

TABLE 1. Dimensionalization of variables. Representative scales for variables $q$, $\psi$, and $t = 1$ are shown as well as the fixed value of model parameters below.

| Dimensionalizing equation | Nondimensional value(s) | Corresponding dimensional value |
|---|---|---|
| $q_{\text{dim}} = qU/L$ ($\text{s}^{-1}$) | $q = 1$ | $q_{\text{dim}} = 1.6 \times 10^{-5}\,\text{s}^{-1}$ |
| $\psi_{\text{dim}} = \psi UL$ ($\text{m}^2\,\text{s}^{-1}$) | $\psi = 1$ | $\psi_{\text{dim}} = 2.6 \times 10^{4}\,\text{m}^2\,\text{s}^{-1}$ |
| $t_{\text{dim}} = tL/U$ | $t = 1$ | $t_{\text{dim}} = 17\,\text{h}$ |
| $\beta_{\text{dim}} = \beta U/L^2$ (m s) $^{-1}$ | $\beta = 0.05$ | $\beta_{\text{dim}} = 2 \times 10^{-11}$ (m s) $^{-1}$ |
| $R_{\text{dim}} = RU/(H_1 + H_2)$ ($\text{s}^{-1}$) | $R_{\text{interior}} = 10^{-6}$ | $R_{\text{interior\_dim}} = 200$ (yr) $^{-1}$ |
| | $R_{\text{sponge}}$ (max) $= 0.1$ | $R_{\text{sponge\_dim}} = 17$ (h) $^{-1}$ |
| $A_{\text{dim}} = AUL$ ($\text{m}^2\,\text{s}^{-1}$) | $A = 3 \times 10^{-5}$ | $A_{\text{dim}} = 1.3\,\text{m}^2\,\text{s}^{-1}$ |
| $H_2 = S_2H_1/S_1$ (m) | $S_1 = 1.0$, $S_2 = 4.0$ | $H_2 = 3200\,\text{m}$ |
| $\eta_{B\_\text{dim}} = \eta_B UH_2/f_0$ (m) | $\eta_B = 4.0$ | $\eta_{B\_\text{dim}} = 2050\,\text{m}$ |

a thickness component proportional to the difference between layer streamfunctions, $(-1)^n(\psi_1 - \psi_2)/S_n$; and a contribution from bathymetry in the lower layer, $\eta_B$. Parameter $S_n$ is the $n$th layer Burger number,

$$S_n = \left(\frac{NH_n}{f_0 L}\right)^2 = \frac{g' H_n}{f_0^2 L^2} = \left(\frac{L_{\text{RO}}}{L}\right)^2,$$

where $H_n$ is the layer depth, $f_0$ is the scale of the Coriolis parameter (about which $f$ is linearized), $N$ is the buoyancy frequency, and $g'$ is the reduced gravity, $g' = g[(\rho_2 - \rho_1)/\rho_0] = N^2 H_n$, where $g$ is gravitational acceleration, $\rho_n$ is the equivalent constant density of the $n$th layer, and $\rho_0$ is a reference density. The reduced gravity is the relevant indicator of stratification in a two-layer system. The Burger number is the squared ratio of the Rossby radius of deformation $L_{\text{RO}}$ and the length scale of motion $L$; it can be thought of as setting the relative depths of the two layers.

The PV conservation equations for the upper and lower layers are

$$\frac{\partial q_n}{\partial t} + J(\psi_n, q_n) - A\nabla^4\psi_n + \nabla \cdot (R_n \nabla \psi_n) = 0, \qquad (2)$$

where $J$ is the Jacobian operator,

$$J(\psi_n, q_n) = \frac{\partial \psi_n}{\partial x}\frac{\partial q_n}{\partial y} - \frac{\partial \psi_n}{\partial y}\frac{\partial q_n}{\partial x} = \mathbf{u}_n \cdot \nabla q_n;$$

$\mathbf{u}_n$ is the horizontal velocity; $A$ is Laplacian viscosity acting on the relative vorticity to suppress grid-scale noise; and $R_n$ is a linear friction coefficient. Parameter $R_2$ has a small background value for numerical stability throughout the domain and increases linearly toward the boundaries in the high-friction sponge layers (Fig. 1; see below and appendix for sponge-layer details). The background value of $R_2$ is the same as in Waterman and Jayne (2011) and is equivalent to a decay time scale of 200 years (Table 1). This is significantly longer than typically accepted bottom friction decay time scales of one year or less (Riviere et al. 2004) and O(15) years (Kondrashov and Berloff 2015). The fact that bottom friction has quantitative effects on circulation is well known (Dewar 1998; Riviere et al. 2004; Venaille et al. 2011), and we will comment on potential consequences of our choice of bottom friction value throughout. Parameter $R_1$ is only nonzero in the high-friction sponge layer, where it has the same sponge friction value as $R_2$.

Nondimensionalization of the model variables requires a choice of scales. Similar to Waterman and Jayne (2011) and Jayne et al. (1996), we choose the following scales: $L = 40\,\text{km}$, $U = 0.64\,\text{m}\,\text{s}^{-1}$, $H_1 = 800\,\text{m}$, and $f_0 = 1 \times 10^{-4}\,\text{s}^{-1}$. These scales set the relationship between the nondimensional and dimensional values of the model variables (Table 1).

The model is forced by flow prescribed at its eastern and western boundaries, where the high-friction sponge layers minimize the effect of the prescribed in- and outflows on the interior dynamics. However, the sponge layer at the western boundary does play a dynamically important role in closing the recirculation gyre momentum and PV budgets. At the northern and southern boundaries, the boundary conditions are no-normal-flow and free-slip. These boundaries are far from the imposed flow so that the effect of the boundary conditions on flow development is insignificant.

The model domain is 6000 km in the north–south direction and 10 000 km from west to east. The model resolution is 4 km, so that the minimum Rossby radius of deformation in the domain, 40 km, is well resolved. Additional model details can be found in the appendix.

In the upper layer, an unstable zonal jet with a Gaussian velocity structure enters the rectangular model domain in the west and exits in the east. The PV associated with the jet changes sign in both the vertical and horizontal (Fig. 2), rendering it unstable to mixed barotropic–baroclinic instability. The meridional structure of PV in the upper layer is dominated by the large PV gradient associated with the jet. As in Waterman and Jayne (2011), the outflow condition specified at the

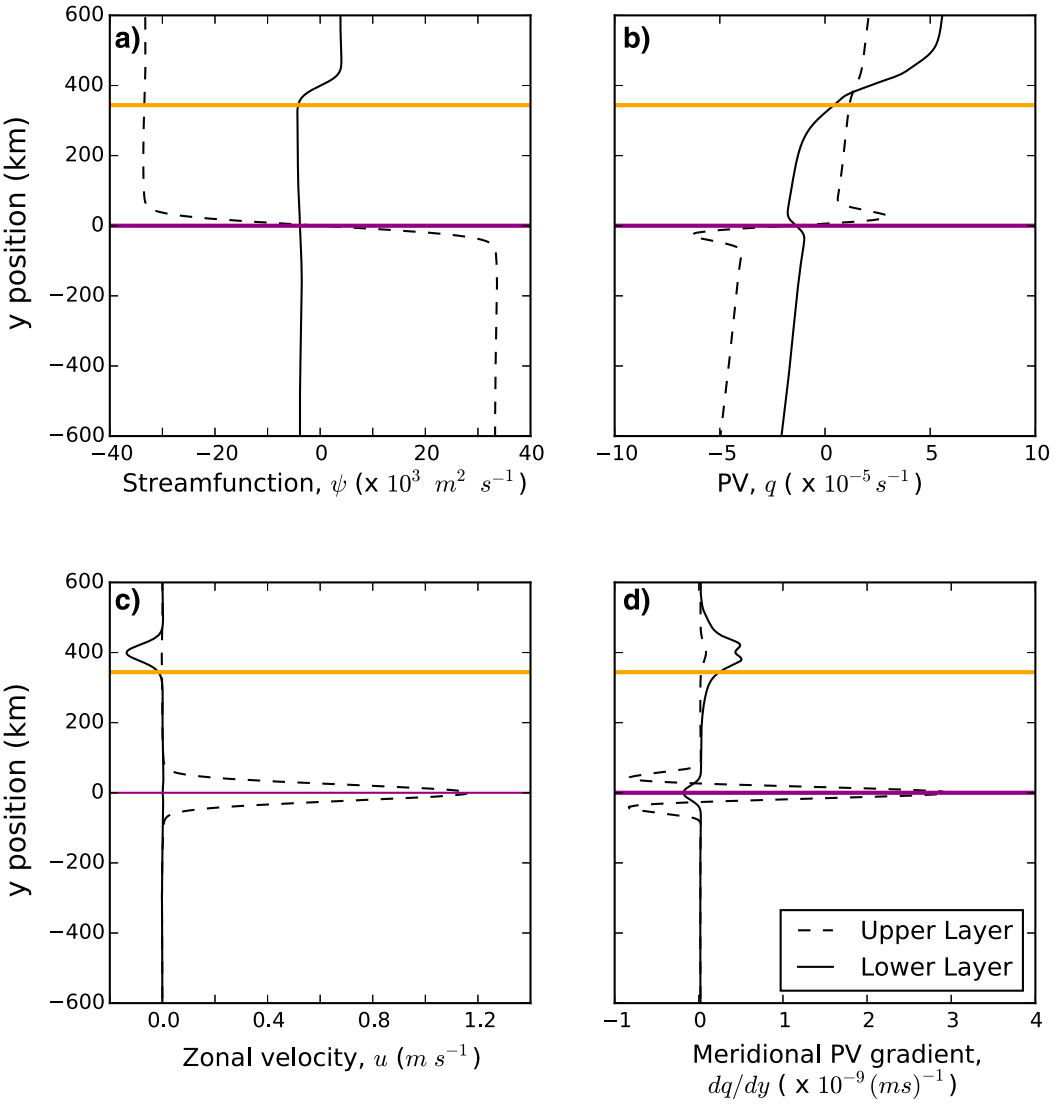


FIG. 2. Meridional structure of the (a) streamfunction $\psi$, (b) PV $q$, (c) zonal velocity $u$, and (d) meridional potential vorticity gradient $dq/dy$ at the model western boundary. Upper-layer properties are dashed and lower-layer properties are solid. A surface-intensified (Gulf Stream like) jet flows eastward in the upper layer and is unstable to mixed barotropic–baroclinic instability as its PV gradients change sign in the horizontal and vertical. In the lower layer, a deep current flows in the opposite direction. The deep current is stabilized by a topographic PV gradient in the lower layer. The horizontal purple line denotes the meridional position of the jet and will be used as a reference point throughout. The horizontal orange line denotes the southern boundary of the deep current.

eastern boundary of the domain is a marginally stable jet profile. The outflow condition is wider and slower than the inflow condition, but they have the same transport so that mass is conserved.

To the north of this jet, in the lower model layer, a deep current flows in the opposite direction: entering the model domain in the east and exiting in the west with the same profile. The deep current has a maximum velocity 9 times smaller than that of the unstable jet, and it travels on a bathymetric slope, which stabilizes the deep current to barotropic and baroclinic instability (Fig. 2).

In our model base case, the imposed transport of the unstable upper layer jet is 55 Sverdrups (Sv; $1\,\mathrm{Sv} = 10^6\,\mathrm{m^3\,s^{-1}}$). In steady state, recirculation gyres form to the north and south of the jet in the upper layer, increasing the transport to 120 Sv at the point of jet stabilization (Fig. 3a). This is analogous to the increase in Gulf Stream transport from 30 Sv in the Florida Straits to 65–95 Sv at Cape Hatteras (Leaman et al. 1989; Meinen and Luther 2016). The speed of the recirculation gyres compares well with observations from Bower and Hogg (1996); in both the model and observations they are $O(10)\,\mathrm{cm\,s^{-1}}$.

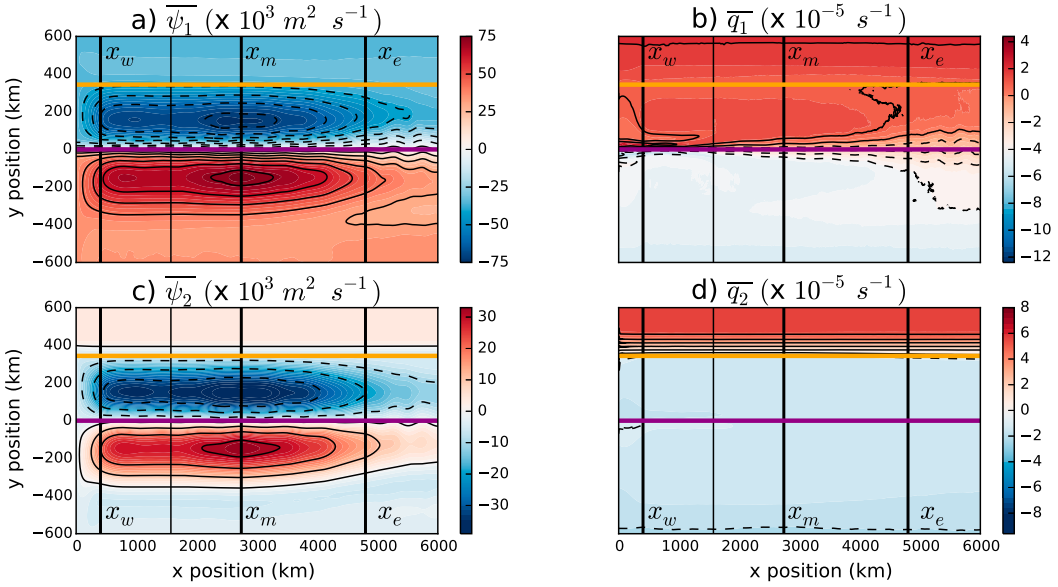


FIG. 3. Mean (left) streamfunction $\overline{\psi}$ and (right) PV $\overline{q}$ in the (top) upper and (bottom) lower layers for the basic model setup, as differentiated by subscripts (1 for upper layer, 2 for lower layer). Thick vertical lines indicate the eastern boundary of the western sponge region, which is the western boundary of our recirculation gyre analyses $x_w$, the zonal position of jet stabilization $x_m$, and the eastern boundary of the recirculation gyre $x_e$. The halfway point between $x_w$ and $x_m$ is also shown, which separates parts 1 and 2 referenced in Fig. 4. The horizontal purple line denotes the meridional position of the jet, and the orange line denotes the southern boundary of the deep current.

After the Gulf Stream separates at Cape Hatteras, it barotropizes and its transport increases to 150 Sv by 60°W (Knauss 1969; Worthington 1976; Hogg 1992). In the model, including the transport that develops in the lower layer adds a further 200 Sv to the total jet transport, rendering it unrealistically large. It may be that the flow field in the deep ocean is too noisy to measure this contribution to the jet transport in the real ocean, or that our model background bottom friction is too weak. As this parameter space was found to be relevant to the Kuroshio (Waterman et al. 2011), and the dynamics of this parameter space is well understood, we proceed with this caveat in mind.

The deep current we impose has a transport of 20.5 Sv in the lower layer, which is consistent with observations of deep DWBC transports at mid- to high latitude (Schott et al. 2006; Zantopp et al. 2017; Toole et al. 2017). Similar to long-term observations of the DWBC at line W at 39°N, the model deep current has a maximum speed of 10 cm $s^{-1}$ and lies between the 2000- and 4000-m isobaths, on the relatively gradual incline of the continental slope offshore of the steep shelf break, which is too steep to simulate in the QG limit. The model continental slope has an error function profile, so that the steepness of the slope has a Gaussian profile as a function of latitude (Fig. 2).

The PV in the lower layer is dominated by the steep meridional gradient due to the bathymetric slope. Within the recirculation gyres to the south of the slope, PV is homogeneous (Figs. 3b,d). This is analogous to the PV structure of the deep ocean within recirculation gyres (Talley and McCartney 1982; McDowell et al. 1982; Bower et al. 1985; Hogg et al. 1986; Lozier 1997). This analogy motivates the zonal model setup: the mean planetary PV contours are overcome by the strong topographic PV gradient and PV homogenization. However, in reality, additional effects are likely present because of the southward component of the DWBC and the weak northward tendency of the Gulf Stream extension.

We use a range of model configurations to gain understanding of the system dynamics. In our model base case (Figs. 2, 3), the inflowing jet velocity is 1.17 m $s^{-1}$ and there are 400 km between the jet and center of the topographic slope. The topographic slope is 200 km wide and 2000 m high in the lower layer. The deep current is centered on the topographic slope.

We vary the inflowing velocity of the jet between 0.36 and 1.43 m $s^{-1}$ and decrease the distance between the jet and the slope from 400 to 250 km by shifting the jet axis northward. Our focus is on jet parameters because they set recirculation gyre properties, and our interest in the distance between the jet and the slope is inspired by observations that the outer edge of the NRG is constrained by bathymetry (Hogg et al. 1986). For each model configuration, we additionally run an equivalent setup without a deep current and one with neither a

deep current nor a topographic slope. The deep current and topographic slope parameters are held constant throughout all model configurations in which they appear.

All model configurations are run for the equivalent of 35 years. We present averages between model years 20 and 35, when the model has reached an approximate steady state.

## 3. Results

### a. *Recirculation gyre dynamics*

In this idealized setup, eddy-mean flow interactions drive inertial recirculation gyres (Waterman and Jayne 2011). Eddies tend to flux PV down the mean PV gradient, due to enstrophy conservation constraints (Rhines and Holland 1979), where enstrophy is defined as the square of eddy PV ($q'^2$). However, if there is a significant local convergence of enstrophy, through eddy decay, for example, eddies can flux PV up the mean gradient.

The nature of the eddy effects depends critically on along-stream position in this model. As the unstable jet enters the domain, it is stabilized by downgradient eddy PV fluxes. Downstream, where the jet has reached marginal stability, eddy enstrophy convergence allows upgradient eddy PV fluxes, which drive the recirculation gyres through nonlinear eddy rectification (Waterman and Jayne 2012). This convergence of eddy enstrophy arises because of the zonal asymmetry in eddy production: eddies are produced upstream in the unstable jet and grow and decay as they are advected by the jet. Once the jet is stabilized by these eddies, it no longer produces eddies, causing a convergence of eddy enstrophy. PV is homogenized by the eddies in the recirculation gyres, so that inertial flow can develop within them.

In the two-layer case, the same mechanism is at play, with some additional complications. In two layers, the jet must be stabilized with respect to both its horizontal and vertical shear. The jet evolution is not significantly altered from the description in Waterman and Jayne (2011) by the addition of the slope and deep current in our model base case presented here.

In the western section of the gyre, the horizontal shear of the jet is dominant, though there are changes in the sign of the PV gradients in both the horizontal and vertical (Fig. 4a). The jet is stabilized with respect to its horizontal shear first, by strong downgradient eddy PV fluxes in the upper layer. Fluxes in the lower layer are also downgradient and increase along the jet axis (Fig. 4b). This increase occurs because momentum has been transferred from the upper layer to the lower layer through thickness fluxes and the vertical shear becomes dominant over the horizontal shear.

The maximum recirculation strength is reached when the jet has been stabilized to both its horizontal and vertical shear. Beyond the point of maximum recirculation, the eddy PV fluxes in the upper layer are weakly upgradient (Fig. 4c), driving the recirculation gyres as in the barotropic case. The eddy thickness fluxes act to make the system more barotropic: in the upper layer the thickness fluxes act against the relative vorticity fluxes to slow the stronger recirculation gyres, and in the lower layer the thickness fluxes accelerate the weaker lower layer recirculations (Waterman and Jayne 2011).

The recirculation gyres are maintained through an approximate balance between mean and eddy flux divergences,

$$\oint \overline{\mathbf{u}}_n \overline{q}_n \cdot \mathbf{dn} \approx \oint \overline{\mathbf{u}'_n q'_n} \cdot \mathbf{dn}, \tag{3}$$

where $\mathbf{u}_n$ is the layer velocity vector, $\mathbf{u}_n = (u_n, v_n) = [-(\partial\psi_n/\partial y), (\partial\psi_n/\partial x)]$, and $\mathbf{dn}$ is the unit vector normal to an integration contour. The viscosity is a small term throughout the domain, and the linear drag is only significant in the high friction sponge layers. In the northern recirculation gyre in the lower layer, where our analysis is focused, the primary PV balance is between a convergence of eddy PV fluxes and a divergence of the mean PV fluxes, or downgradient eddy PV fluxes balanced by an upgradient mean flux of PV.

The convergence of eddy PV flux is dominated by meridional eddy PV fluxes. The zonally integrated meridional eddy PV fluxes are positive at the jet center and negative at the northern extent of the recirculation gyre, resulting in an eddy PV flux convergence (Fig. 5b). The unstable jet sheds eddies that homogenize PV from the jet axis. These eddies first homogenize the meridional PV profile to the jet's negative PV gradient and then to the positive planetary PV gradient to the north of the jet (Fig. 5a). The PV gradient in this region becomes ever steeper as PV is homogenized farther north, creating an ever-larger barrier to the homogenizing eddies, which flux PV less effectively as they get farther from the jet.

The mean PV flux divergence that balances the eddy PV flux convergence of the northern recirculation gyre is associated with the northern edge of the westward return flow of the northern recirculation gyre, which occurs on the PV gradient to the north of the homogenized region (Fig. 5c). This corresponds to a mean upgradient PV flux, since the recirculation gyre waters originate from the homogenized region with lower PV. In summary, the eddy PV flux convergence due to the downgradient PV fluxes at the jet center and at the gyre's northern boundary are balanced by the mean PV

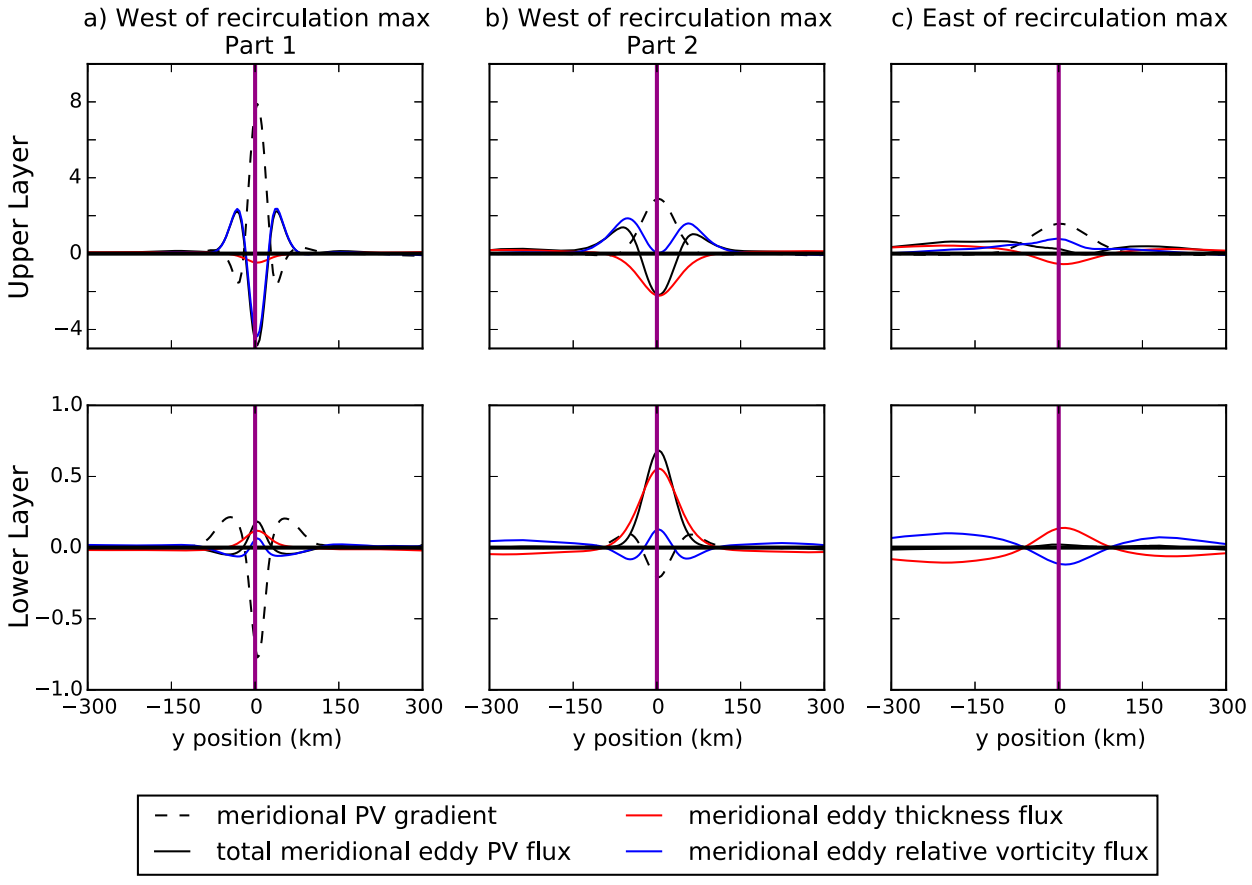


FIG. 4. Normalized meridional PV gradients $dq/dy$ and meridional eddy PV fluxes $\int \overline{v'q'}\,dx$ for three primary sections of the recirculation gyre depicted in Fig. 3. Zonal average between (a) $x_w$ and $(x_m + x_w)/2$, (b) $(x_m + x_w)/2$ and $x_m$, and (c) $x_m$ and $x_e$. Upper-layer properties are shown in the top row, and lower-layer properties are in the bottom row. PV gradients and eddy fluxes are normalized consistently so that quantities of each can be compared between panels. Note the difference in scale between the upper- and lower-layer panels. Vertical purple lines denote the meridional position of the jet.

flux divergence associated with the mean upgradient PV flux within the northern recirculation gyre.

When a slope is added within the natural extent of its recirculation gyre, this balance is achieved at a more southerly position, with larger eddy PV fluxes down the topographic PV gradient (Fig. 5b). The mean PV flux, which balances this increased eddy PV flux, is larger as there is zonal return flow on the bathymetric slope, which has high PV (Figs. 5a,c).

### b. *The meridional extent of recirculation gyres*

We can use this understanding to derive an analytic solution for the PV distribution in the lower layer of the present model. PV is homogenized about the center of jet. Because PV increases to the north of the jet and decreases to its south, and the eddies homogenize symmetrically about the center of the jet, the final PV in the homogenized region in the lower layer will be the initial PV at the center of the jet (Fig. 5a). As in Jayne et al. (1996) and Jayne and Hogg (1999), we apply the ad hoc assumptions that meridionally integrated PV is conserved, and that the PV structure beyond the homogenized region remains unchanged, giving an equation for the northern extent of the recirculation gyre in the lower layer $y_r$ in terms of known quantities:

$$\int_{y_j}^{y_r} q_{2,\mathrm{init}}(y)\,dy = q_{2,\mathrm{init}}(y_j) \times (y_r - y_j); \qquad (4)$$

$y_j$ is the meridional position of the center of the jet and $q_{2,\mathrm{init}}(y)$ is the initial meridional profile of PV in the lower layer. In this conceptual model, the extent of PV homogenization and the intersection of the initial and steady-state profiles are equivalent, and there is a discontinuity in PV at this point. However, in the QG model, there is a region with a finite PV gradient between the northernmost extent of PV homogenization and the intersection of the initial and homogenized PV profiles (Fig. 5a). It is in this region that the gyre's return flow supplies the mean PV flux divergence discussed in the previous section.

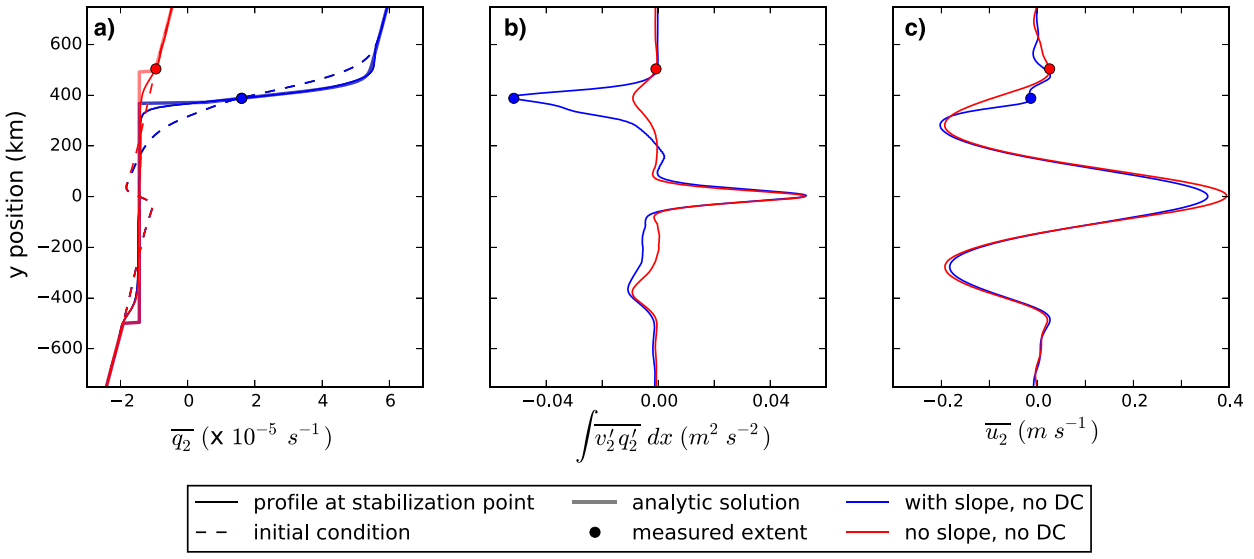


FIG. 5. Profiles of (a) time mean PV in the lower layer $\overline{q_2}$, (b) integrated meridional eddy PV flux $\int_{x_w}^{x_e} \overline{v_2' q_2'}\, dx$, (c) and zonal velocity at $x_m$, $\overline{u_2}(x_m)$. Blue lines denote model configurations with a topographic slope in the lower layer and red denotes model runs without. Neither model configuration includes a deep current (DC). In (a), the initial profile imposed at the western boundary is denoted with a dashed line; $\overline{q_2}(x_m)$ with a solid line; and the predicted, discontinuous homogenized profile with a thick, semitransparent line, as differentiated using black lines in the legend. The meridional eddy PV flux shown in (b) is integrated zonally from $x_w$ to $x_e$. In (a)–(c), points indicate the measured northern edge of the recirculation gyres, defined as the intersection of the solid and dashed lines in (a).

Because of this difference, $y_r$ actually corresponds to a point between the extent of the region of homogenized PV and the intersection of the initial and final PV profiles, complicating the testing of this analytic prediction. We define the extent of the recirculation gyre in the lower layer as the $y$ position of the intersection of the $q_{2,\text{init}}$ and $\overline{q_2}(x_m)$, the time mean PV at the point of jet stabilization.

There is a general correspondence between the predicted value and measured extent of the northern recirculation gyre for all model configurations (Fig. 6). This holds even when the model configuration includes a slope and deep current, suggesting that the order one dynamics are relatively unchanged by their addition. There is increasing discrepancy between predicted and measured recirculation gyre extents for model cases with slower inflowing velocities because the eddies in these model cases are less effective at homogenizing PV. This results in a weaker PV gradient between the region of homogenized PV and the initial PV profile and does not conform well with our predicted PV profile, in which there is a steep gradient in PV between the homogenized region and the initial PV profile.

### c. *Stirring of the deep current*

Eddy PV fluxes at the northern edge of the recirculation gyre increase when a slope is added within the natural extent of the recirculation gyre (Fig. 5b). In model configurations with a deep current along the topographic slope, the eddy PV flux at the recirculation gyre–deep current interface remains elevated. These eddy PV fluxes stir the deep current with interior recirculation gyre waters, as has been observed for the DWBC in the North Atlantic, for example (Bower et al. 2009; Le Bras et al. 2017).

The eddy PV fluxes at the recirculation gyre–deep current interface increase as the jet's inflowing velocity is increased (Fig. 7b). A faster inflowing jet velocity corresponds to a more unstable jet as both vertical and horizontal shear are increased. The energetic eddies created by more unstable jets are associated with a larger PV flux down the jet's PV gradient. By the time they reach the topographic slope, which is 400 km to the north of the jet in each of these model configurations, they are more energetic than in less unstable cases, causing a larger downgradient meridional eddy PV flux at the edge of the recirculation gyre. If the topographic slope was not present, the more unstable jets would drive recirculation gyres with naturally larger meridional extents, as shown in the previous section. For more unstable jets, the recirculation gyre homogenizes farther into the deep current, so that the recirculation gyre and deep current are less distinguishable (Fig. 7a).

Changing the distance between the jet and topographic slope has little effect on the deep current's velocity profile (Fig. 8a). However, in model configurations with less distance between the jet and the topographic slope, eddy PV fluxes at the base of the slope are dampened (Fig. 8b). This result is counterintuitive, as

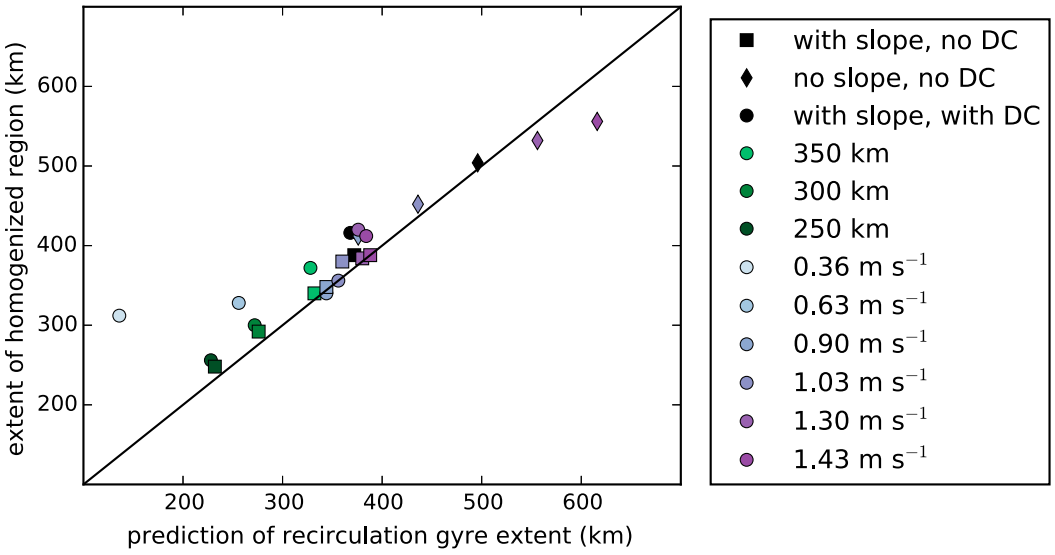


FIG. 6. Analytic meridional recirculation gyre extent prediction against measured meridional extent in the QG model (both in km). Marker shape differentiates whether a slope or deep current (DC) are present in the model configuration. Color differentiates model configurations with varying inflowing jet velocity (purple) and distance between the jet and slope (green) relative to the base cases (black), as described in the legend. The meridional extent in the QG model is defined as the $y$ position at which $q_{2,\text{init}}$, the $q_2$ profile imposed at the western boundary, and $\overline{q_2}(x_m)$ intersect. The diagonal black line is the $y = x$ line for reference.

the jet is initialized with the same inflowing velocity in each of these model cases. If anything, one might expect that the eddy PV flux at the base of the slope would be elevated when the jet is closer to the slope, as the eddies produced by the jet would be closer to their source and therefore more energetic. However, proximity to the slope causes feedbacks on the jet's instability, as we describe in the following section.

### d. *Feedbacks on jet instability*

The zonal jet evolution is more stable in model cases with less meridional distance between the jet and the

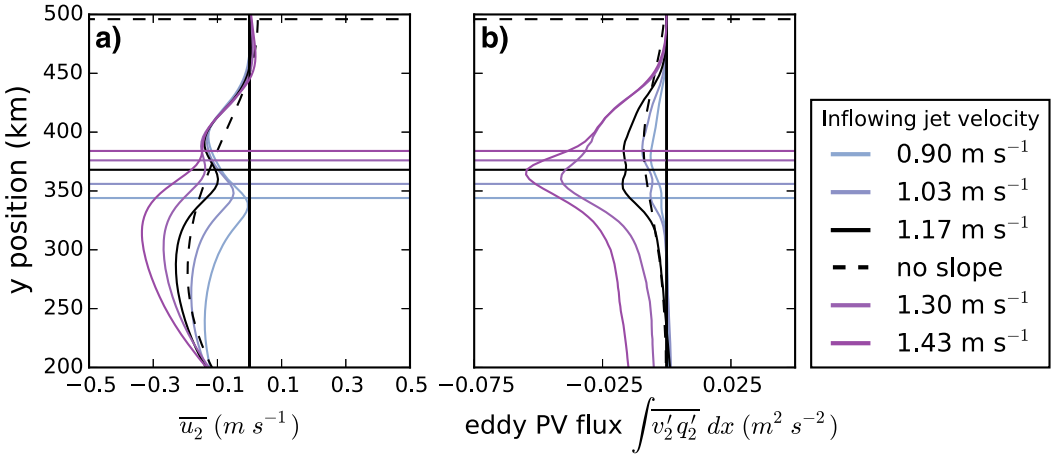


FIG. 7. Meridional structure of (a) the time mean zonal velocity in the lower layer $\overline{u_2}$ at $x_m$ and (b) the cumulative meridional eddy PV flux $\int_{x_w}^{x_e} \overline{v_2' q_2'}\ dx$ for model configurations with varying inflowing jet velocities, as specified in the legend. Solid lines denote model runs that include a topographic slope and deep current, and dashed lines show the model base case (black) without a slope for reference. Predicted recirculation gyre extents for each model configuration are denoted with a horizontal line in both panels in the same color/style. Model runs with a faster inflowing jet velocity and hence more unstable jet have faster northern recirculation gyre return flows and larger meridional eddy PV flux at the recirculation gyre–deep current interface.

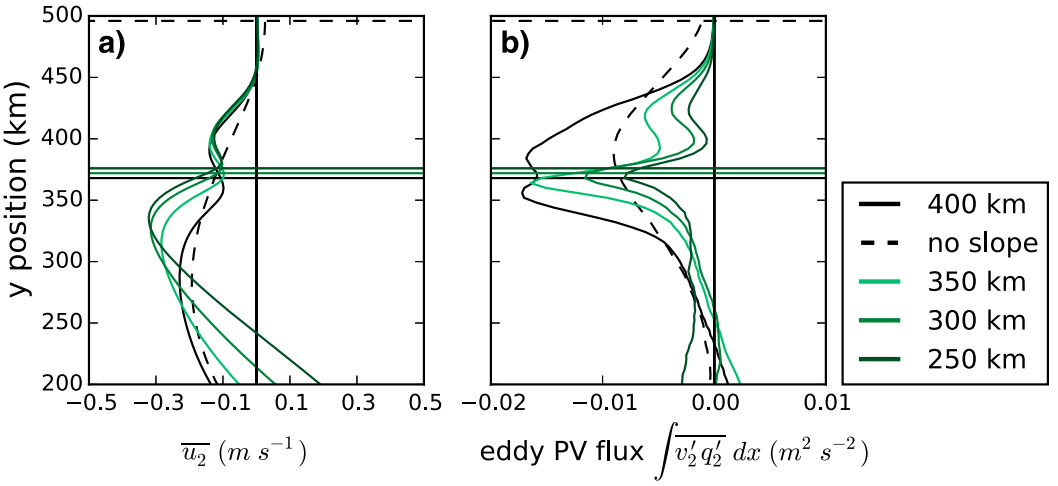


FIG. 8. As in Fig. 7, but for model configurations with varying distances between the unstable jet and deep current, as specified in the legend. As before, solid lines denote model runs that include a topographic slope and deep current, dashed lines show the model base case (black) without a slope for reference, and horizontal lines in both panels indicate the predicted extent of the recirculation gyre. The meridional eddy PV flux at the recirculation gyre–deep current interface decreases with proximity of the currents.

slope. This is reflected in the net meridional eddy PV flux at the jet axis, which decreases with proximity between the jet and slope (Fig. 9b). The cumulative meridional eddy PV flux along the jet axis is composed of three primary stages (Fig. 9a). First, there is a gradual slope in the western area of the domain, where the eddies are growing to finite amplitude as they are advected by the jet (stage 1), and then a constant, steeper slope, where the eddies are fluxing PV at a constant rate (stage 2). Finally, once the jet has been stabilized, the eddies flux PV upgradient at a very low rate, which is evident in the slight decrease in cumulative meridional PV flux after the maximum has been reached (stage 3).

The distinction between model configurations with different distances between the unstable jet and the topographic slope (Fig. 9b) is primarily due to a difference in the initial slope of the cumulative meridional eddy PV flux (stage 1), when the eddies are growing, which indicates that the eddy growth rate is suppressed by the addition of the bathymetric slope. The slopes of the cumulative meridional eddy PV flux in the second stage, when the eddies are fluxing PV at an elevated, constant rate are much more similar than during this initial growth period.

These differences in recirculation gyre forcing patterns are also reflected in the geometry of the recirculation gyre flow patterns. The recirculation gyre extends in the zonal direction when the distance between the jet and the slope decreases (Figs. 10b,c). This change in geometry is consistent with the hypothesis in Waterman and Jayne (2011) that the zonal length of the recirculation gyre is determined by how quickly eddies grow to an efficient PV fluxing size as they are advected by the jet; when eddies grow more slowly, the jet is stabilized farther downstream. Note also that the shape of the southern recirculation gyre changes in concert with the northern gyre (Fig. 10), as the effects are communicated through eddy PV fluxes at the jet center.

The cumulative meridional eddy PV flux reaches a lower net value in jets that are closer to the topographic slope. This leads to a weakening in the strength of the recirculation gyres, and standing meanders in the jet become apparent (Fig. 10c). In these cases, the cumulative eddy PV fluxes are not sufficient to stabilize the jet, and the recirculation gyres extend zonally to the eastern high-friction sponge region. If the background bottom friction was larger, these cases may not arise, as bottom friction could remove substantial energy from the recirculation gyres within the model interior domain. In general, the recirculation gyres would be weaker and smaller with higher bottom friction.

Model snapshots of upper-layer PV $q_1$ also indicate a qualitative change in properties with proximity to the slope (Fig. 11). Coherent eddies and meanders appear to decrease in size when the unstable jet is closer to the slope. We show the upper-layer PV field, as the eddy characteristics are similar in the upper and lower layer, but the eddies in the vicinity of the jet are more visible in the upper-layer PV field because of the PV gradient at the jet axis.

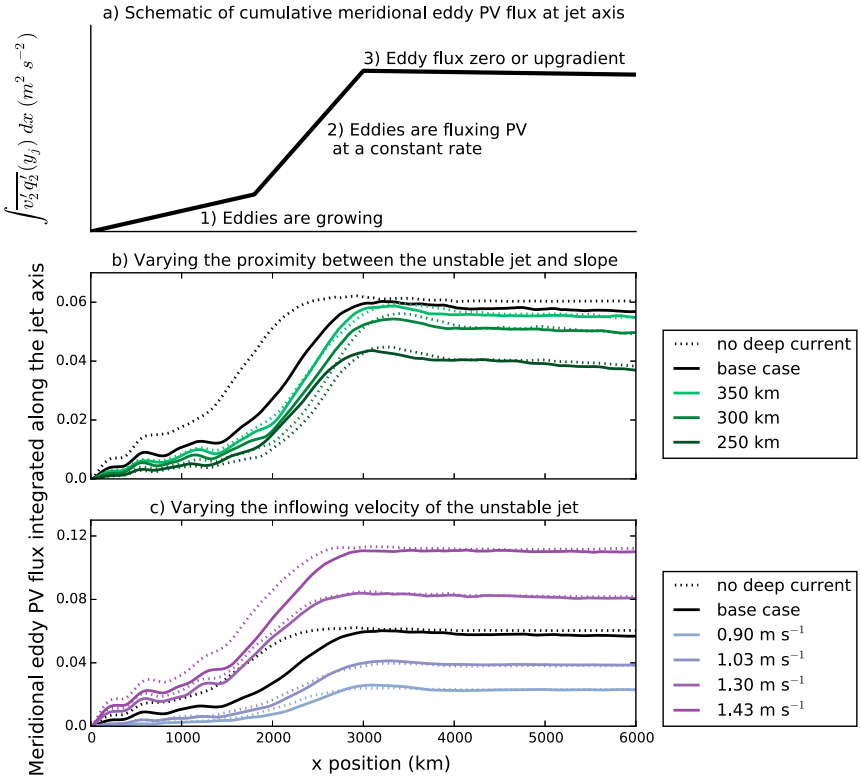


FIG. 9. Lower-layer cumulative meridional eddy PV fluxes integrated zonally along the jet axis, that is, $\int_0^x \overline{v_2' q_2'}(y_j)\,dx$ as a function of zonal position $x$. (a) Schematic showing how the three primary stages of eddy behavior are reflected in this quantity. (b) When the unstable jet is closer to the topographic slope, the eddy growth rate is dampened (stage 1) and the net cumulative eddy PV flux of the jet decreases. (c) When the inflowing jet velocity is increased, the eddy growth rate (stage 1), the eddy fluxing rate (stage 2), and the net cumulative eddy PV flux all increase. Model runs that include a deep current are depicted in solid lines and those without a deep current are depicted in dotted lines. In the model base case in particular, the deep current dampens the eddy growth rate (stage 1).

To investigate this further, we calculated the linear stability characteristics of the model setup. We started from the linearized PV conservation equation,

$$(\overline{u_i} - c)\tilde{q}_i' + \overline{q}_{iy}\tilde{\psi}_i' = 0, \tag{5}$$

where primes indicate small wavelike perturbations with the form $q_i' = \tilde{q}_i'(y)\,e^{ik(x-ct)}$, so that the tilde denotes magnitude of the perturbation, which is a function of $y$. Overlines indicate the basic state that we linearize around. We used the definition of $\psi$ as a function of $q$ to form an eigenvalue problem for $\tilde{q}_i'$, where the eigenvalues correspond to $c$, and the eigenvectors are the corresponding meridional structure of $q$ perturbations $\tilde{q}_i'(y)$. We applied this analysis to the prescribed inflowing jet $u$ and $q$ profiles and for time mean profiles at 1000 and 1600 km downstream for the model configurations shown in Fig. 10. We found that the suppressed eddy growth could not be explained using this linear stability analysis: the meridional structure of the most unstable mode is restricted to the meridional width of the jet, which does not intersect with the slope.

Linear stability analysis does not account for what occurs to the instabilities as they grow and become large enough to interact with the slope. This is probably why it does not explain the suppression of eddy growth when a slope is added to the domain. We are also assuming that it is sensible to linearize the jet around its time mean state, and we do not take zonal changes in jet structure into account. This analysis indicates that the suppression of eddy growth in this model is likely a nonlinear process, and further investigation presents an exciting avenue for future work.

In most model configurations, the jet's eddy growth rate is decreased when a deep current is present (Fig. 9c). This effect is particularly pronounced for the model base case, perhaps because the meridional distance between the jet and the slope is approximately the

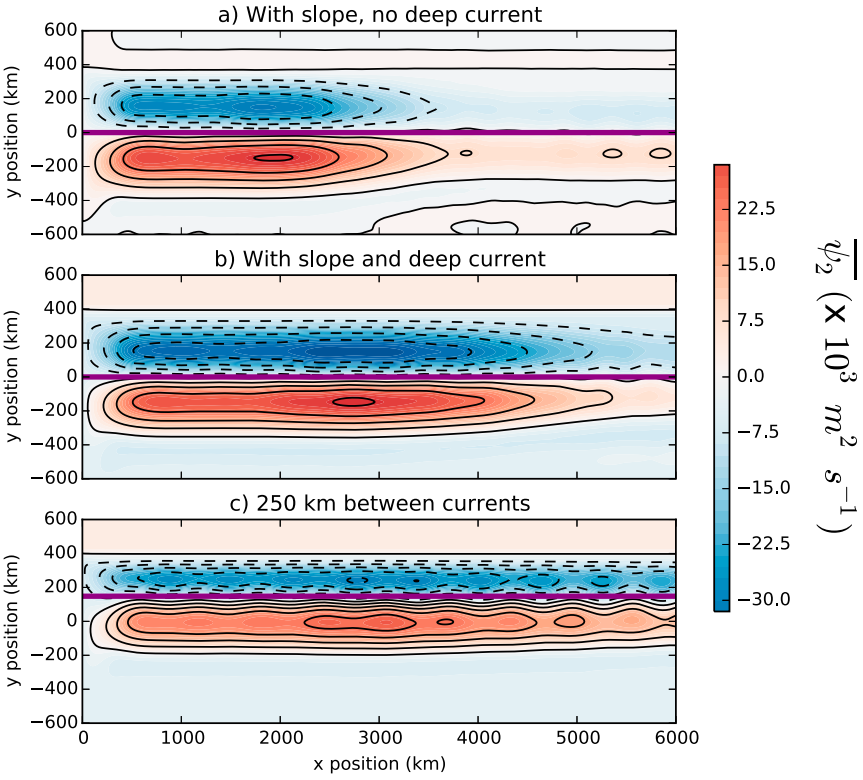


FIG. 10. Time mean streamfunction in the lower layer $\overline{\psi}_2$ for the model base case (a) with a slope but no deep current, (b) with a slope and a deep current, and (c) for a model configuration with 250 km between the jet and deep current [closer than the 400 km in (b)]. Horizontal purple lines indicate the meridional position of the jet axis. The recirculation gyres are elongated zonally when the eddy growth rate is dampened.

same as the natural meridional extent of the recirculation gyre in the base case model configuration. This is also reflected in the geometry of the recirculation gyres: when there is a deep current on the slope, the recirculation gyre is longer in the zonal direction, as the eddies are growing more slowly and it takes a longer zonal distance to stabilize the jet (Figs. 10a,b and 12a,b). In model cases with small distances between the jet and the slope, the deep current has a slight destabilizing effect. The effect of the deep current similarly cannot be explained through our linear stability analysis. The deep current itself is stable in all model configurations; it has identical initial conditions in all configurations and is always stabilized by the topographic slope on which it flows.

### *e. Deep current transport*

We impose the deep current transport through model boundary conditions, but in the interior the flow field contends with the recirculation gyre circulation system. In our model, the northern recirculation gyre can homogenize PV into the topographic slope and distort the velocity profile of the deep current on the slope (Figs. 7a, 8a). This has implications for measuring the transport of deep currents adjacent to recirculation gyres, as the two circulation systems are almost indistinguishable: there is no zero crossing of velocity between the two.

The zonal transport at deep current latitudes is primarily a superposition of the imposed deep current transport and the recirculation gyre return flow (Fig. 12). This can be deduced as the transport anomaly follows the same pattern whether or not a deep current is present. The suppression of eddy growth by the deep current for the model base case and more unstable model configurations (Fig. 9c) is also apparent in that the recirculation gyre transport signature is more zonally elongated when a there is a deep current in the model configuration.

As the transport signature of the deep current is a superposition of the imposed transport and recirculation gyre flow, the meridionally integrated transport changes significantly as the deep current encounters the recirculation gyre, then is relatively constant as it runs adjacent to the recirculation gyre. In the North Atlantic, this adjustment for the Northern Recirculation Gyre likely occurs at the Tail of the Grand Banks, where increased interaction between the deep western boundary

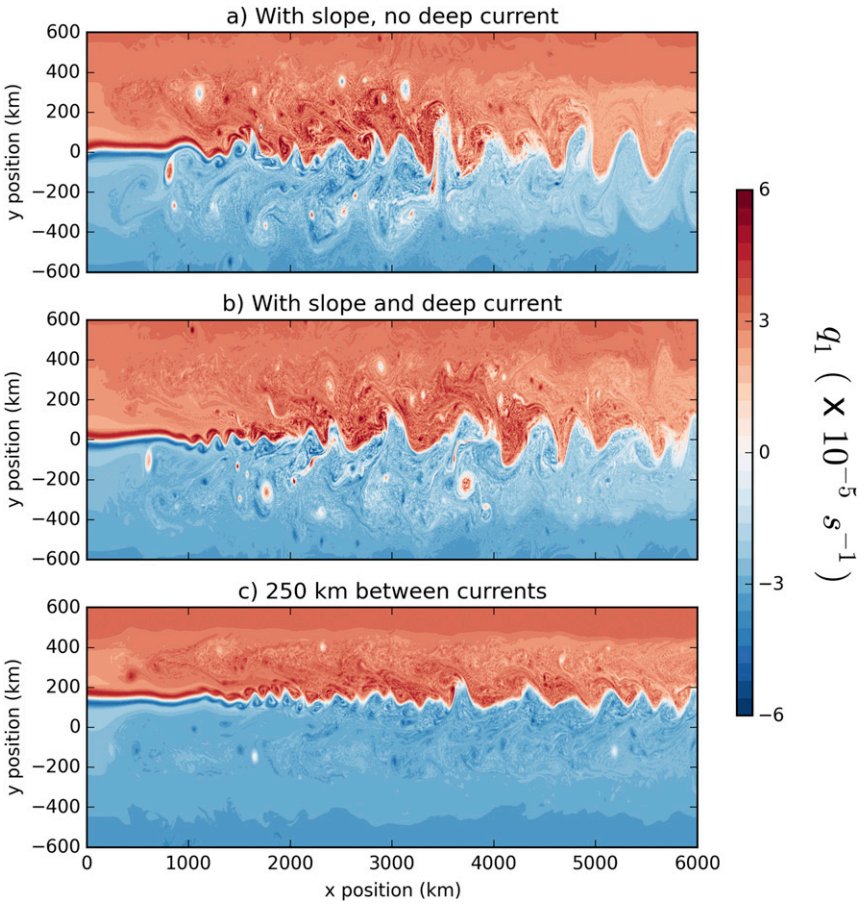


FIG. 11. Snapshots of upper layer PV $q_1$ for the same model configurations as in Fig. 10, the model base case (a) with a slope but no deep current, (b) with a slope and a deep current, and (c) the model configuration with 250 km between the jet and deep current [closer than the 400 km in (b)]. There appears to be a shift in character to a less active eddy field and smaller meander scales in (c), consistent with the decrease in eddy growth rate and net meridional eddy PV flux shown in Figs. 9 and 10.

current and the interior of the North Atlantic has been observed (Bower et al. 2009; Le Bras et al. 2017).

## 4. Discussion

Motivated by the circulation in the North Atlantic, we used an idealized two-layer quasigeostrophic model to investigate the adjustment of a recirculation gyre to a topographic slope at depth. Our analysis focuses on the parameter space in which the size of recirculation gyre is limited by seafloor bathymetry, as is the case in the North Atlantic (Hogg 1992; Lozier 1997; Zhang and Vallis 2007). The coexistence of the Northern Recirculation Gyre (NRG) and deep western boundary current (DWBC) at depth was observed by Hogg (1983), and Lagrangian studies suggest a flux of properties between them (Bower et al. 2009; Gary et al. 2011).

In our model, the northern recirculation gyre is constrained meridionally by a bathymetric slope when the slope is closer to the jet axis than the natural meridional extent of the recirculation gyre. We predict the meridional extent of the gyre using the assumption that the meridional integral of PV is conserved, as in Jayne et al. (1996), and find that the recirculation gyre can homogenize PV into the topographic slope. The PV balance of the northern recirculation gyre in the lower layer is between a mean PV flux divergence and an eddy PV flux convergence. When a slope is added in the lower layer, eddy PV fluxes at the base of the slope increase. These increased eddy PV fluxes stir the deep current flowing westward on the slope with the recirculation gyre waters to its south.

When the inflowing jet velocity is increased, eddy PV fluxes at the recirculation gyre–deep current interface increase. Additionally, more unstable jets homogenize

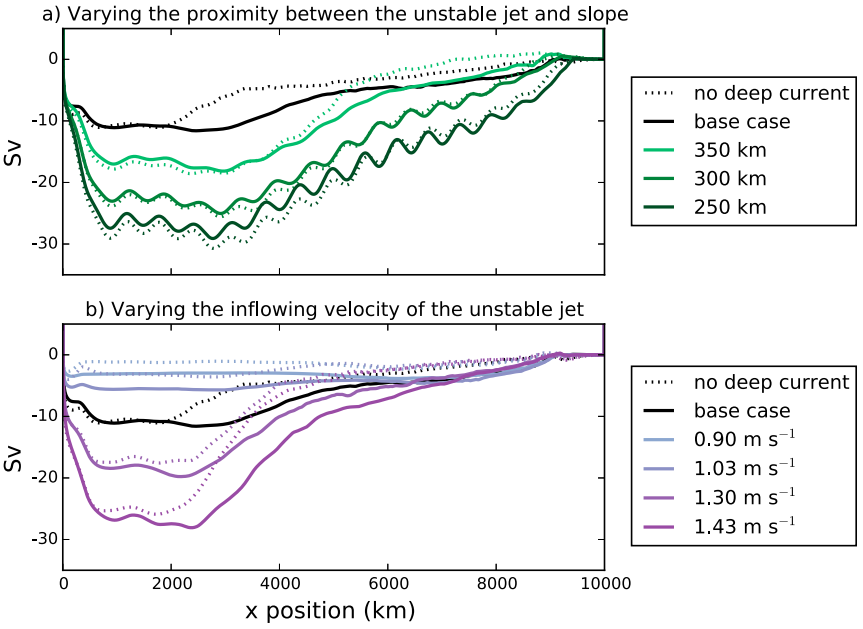


FIG. 12. Time-mean anomalous westward transport at deep current latitudes (north of $y$ = 350 km, orange line in Figs. 2, 3) as a function of zonal position. Model configurations with a deep current are depicted in solid lines and those without in dotted lines. Colors highlight the model features that distinguish it from the base case, (a) the meridional distance between the unstable jet and topographic slope and (b) the inflowing velocity of the jet, as described in the legends. In cases with a deep current, the mean imposed transport of 20.5 Sv has been subtracted. In general, the anomalous transport mirrors the northern recirculation transport whether there is a deep current in the model configuration or not, implying both that the deep current is largely passive and that most transport convergence occurs on the eastern side of the recirculation gyre. In more unstable model runs, the deep current acts to stabilize the recirculation gyre, causing a zonal elongation of the recirculation gyre in cases with a deep current.

PV further into the slope and alter the deep current's velocity structure more significantly. However, when the jet axis is moved northward, toward the slope, there is little effect on the deep current's velocity structure, and the eddy PV flux at the base of the slope is dampened. This dampening of eddy PV flux originates at the jet axis, where we show that the eddy growth rate decreases with proximity to the slope. This effect is not explainable by a linear stability analysis and is likely linked to nonlinear eddy growth. In the North Atlantic, this effect has implications for the Gulf Stream extension, whose instability may be dampened by the proximity of the NRG and the continental slope.

The transport at deep current latitudes is a linear superposition of the imposed deep current transport and the recirculation gyre transport, which suggests a largely passive role for the deep current (Fig. 12). At the same time, in more unstable model configurations, the deep current dampens eddy growth in the unstable jet, elongating the recirculation gyres zonally (Figs. 9, 10). As the transport signature of the deep current mirrors the recirculation gyre transport, this suggests a rearrangement of mass that may also occur in reality as the DWBC rounds the Tail of the Grand Banks and reaches the NRG. Lagrangian studies implicate the Tail of the Grand Banks as a location at which there is heightened stirring between the DWBC and the interior (Bower et al. 2009; Gary et al. 2011), and it is receiving growing attention as a climatically significant transition point (Buckley and Marshall 2015).

In many of our model configurations, there is no zero crossing of the zonal velocity between the deep current and recirculation gyre. This potential merging has significant consequences for the interpretation of moored boundary arrays that monitor the DWBC in the North Atlantic, where the DWBC is hard to define because of its proximity to the Gulf Stream and NRG (e.g., Toole et al. 2011, 2017).

The reported consequences for the deep current in our model are generally dependent on the position, width, and strength of the deep current. For example, a deep current that is positioned farther upslope than in

the configurations presented here may not merge with the recirculation gyre and be out of reach of the eddy PV fluxes at the base of the slope.

Adding a slope to the south of the recirculation gyres would not necessarily have all the same effects as adding the slope to the north. While we would expect a slope to the south to constrain the size of the southern recirculation gyre and cause downgradient fluxes that could stir the deep current with the interior, the sign of these eddy fluxes would be in the opposite direction as those at the edge of the southern recirculation gyre, unlike in the northern recirculation gyre case.

Eddy PV fluxes have not previously been reported in observations or models at the edge of the NRG. Xu et al. (2015) found off-slope eddy *tracer* fluxes in a high-resolution model at the Flemish Cap, just north of the Tail of the Grand Banks. This indicates that off-slope eddy fluxes could be significant more generally where there are large eddy fields, and our model framework could be used to interpret the dynamics of this interaction further. Bower and Hogg (1992) and Hogg (2000) caution that model–data comparisons of eddy fluxes are particularly challenging, as eddy fluxes are both difficult to measure and sensitive to model particularities.

In Gary et al. (2011), particles that leave the DWBC travel southward in a broad region encompassing both recirculation gyres. In our model, once DWBC water is stirred into the interior, it circulates with the northern recirculation gyre. So, though the properties can spread throughout the recirculation gyres, water only flows in the same direction as the deep current in the northern half of the NRG, not throughout both gyres. This is similar to the effect in the simple model presented in Hogg et al. (1986) to explain the tongue of DWBC water in the interior due to stirring with the NRG.

Our idealized quasigeostrophic model framework allows us to isolate the dynamics of the system. However, this simplicity also limits the scope of our results. For example, small irregularities in bathymetry, submesoscales, and bottom boundary layer dynamics may play an important role in reality and are not resolved in our model. The QG approximation is also limiting for this application because it does not allow vanishing layer thicknesses or very steep topography. This limits the model deep current to one layer, which is analogous to the deep overflow water component of the DWBC.

Observations and past modeling work indicate that a three-layer model representation of the DWBC is preferable because of the differences in the water mass components of the DWBC (Pickart and Smethie 1993; Spall 1996). In particular, the present model lacks a layer analogous to the intermediate Labrador Seawater, which would likely complicate the dynamics of the system because of its low PV signature. In Spall (1996), the intermediate Labrador Seawater layer shelters the deepest layer from layer thickness changes when the DWBC flows under the Gulf Stream. If a third layer were added to our configuration, the interaction between the DWBC and the NRG would likely be more significant in an intermediate layer, where the eddy energies would be larger.

In the present model, a field of eddies is forced by an unstable jet, but the effect of each individual eddy on cross-slope exchange was not explored. Recent work by Cherian and Brink (2016) focused on the effect of individual eddies on cross-shelf exchange, using the beta effect to propel eddies into a slope. They emphasize the differences in behavior for anticyclonic and cyclonic eddies and found a cross-slope stirring mechanism that results in subsurface exchange. We do not reproduce this mechanism, likely because of our limited vertical resolution, and we have not found differences in behavior between anticyclonic and cyclonic eddies. There remain many interesting questions at the interface of these two studies.

We explored the dynamics of the interaction between recirculation gyres and a deep boundary current on a topographic slope. We found that the recirculation gyre's adjustment to the slope leads to increased eddy PV fluxes that stir the deep current with the interior and identified feedbacks on the unstable jet that drives the recirculation gyres. These mechanisms may shape the circulation in the western North Atlantic, and this work provides a framework for future work in high-resolution models of the North Atlantic as well as observations.

*Acknowledgments.* We gratefully acknowledge an AMS graduate fellowship (IALB) and U.S. National Science Foundation Grants OCE-1332667 and 1332834 (IALB and JMT). We thank Glenn Flierl for his assistance with the linear stability analysis, Stephanie Waterman for her insights regarding eddy growth rates, Michael Spall for his guidance in conceiving this study, Harriet Alexander for her help with Fig. 1, and Amy Bower for interesting discussions about the implications of this work.

## APPENDIX

### Additional Model Details

As described in Waterman and Jayne (2011), the model solves the barotropic and baroclinic PV equations, which are equations for $(q_1/S_1 + q_2/S_2)$ and $(q_1 - q_2)$, respectively. Details on the numerical method

can be found in Waterman and Jayne (2011) and Jayne and Hogg (1999). The time stepping is done using a third-order Adams–Bashforth scheme (Durran 1991), integration in time and space is done using an Arakawa A-grid, and advection terms are calculated using the Arakawa (1966) vorticity-conserving scheme. To solve for the streamfunction at each time step, the relative vorticity is inverted using the generalized Buneman algorithm (Adams et al. 1988). Eddy flux terms are accumulated while the model is running, so that there are contributions from each time step.

There are several notable differences between our model setup and that used in Waterman and Jayne (2011) beyond those intrinsic to our scientific questions, the addition of a topographic slope, and deep current in the model lower layer. In this model configuration, there is no sponge layer in the north or south of the domain. The western and eastern sponge layers are as in Waterman and Jayne (2011), 100 grid points wide in the west and 200 in the east of the domain. In each sponge layer, the linear friction coefficient $R$ is ramped up linearly from the background value to its maximum value (0.1) at the domain boundary.

In our model framework, we have decreased the time step from 0.04 ndu (nondimensional units) to 0.025 ndu. The set of model runs with the fastest inflowing jet velocity ($1.43\,\mathrm{m\,s^{-1}}$) have a time step of 0.02 ndu for numerical stability. We have added viscosity, as described in section 2, to suppress grid-scale noise and smooth time-averaged fields and fluxes. We also added dependence of the linear friction on gradients in the linear friction coefficient $R$, that is, we changed the term in Eq. (2) from $R\nabla^2\psi$ to $\nabla\cdot(R\nabla\psi)$.

The geometry of the model domain is also distinct. Our domain is longer in the zonal direction: 250 ndu instead of 150 ndu. This is because the addition of the slope in the lower layer can stretch the recirculation gyres in the zonal direction.

We found that the model behavior is sensitive to the value of the constant viscosity parameter $A$, which determines the size of the diffusion intended to suppress grid-scale noise. Significantly, an increase in $A$ decreases the relative vorticity of the DWBC, which is not realistic. Large viscosity also suppresses homogenization into the slope, as sharp gradients in relative vorticity are smoothed out by the viscosity. We ran the model in the base case configuration with nondimensional values of $A = 3\times10^{-4}$, $1\times10^{-4}$, $3\times10^{-5}$, and $1\times10^{-5}$, which correspond to dimensional values of 13, 4.3, 1.3, and $0.4\,\mathrm{m^2\,s^{-1}}$, respectively. Our chosen value of $A = 1.3\,\mathrm{m^2\,s^{-1}}$ does not smooth out the DWBC but does suppress grid-scale noise.

We also found that the shape of the recirculation gyres is sensitive to the value of this parameter, with higher viscosity lengthening the recirculation gyres in the zonal direction, as shown in Le Bras (2017). This is likely because the viscosity smooths the relative vorticity of the jet, decreasing the instability of the jet as well as the eddy fluxes. This change is analogous to the sensitivity of gyre shape to jet instability discussed in section 3.

In Waterman and Jayne (2011), the instability is altered by changing the nondimensional $\beta$ of the system. Here we change the initial strength of the jet, so that the ratio between the planetary and bathymetric PV gradients remains constant. We vary the inflowing jet strength in the upper layer from 0.36 to $1.43\,\mathrm{m\,s^{-1}}$, which is similar to the range explored in the two-layer model in Waterman and Jayne (2011) ($0.01$–$1\,\mathrm{m\,s^{-1}}$). The Waterman and Jayne (2011) two-layer model configurations correspond to nondimensional beta between 0.02 and 0.6, which overlaps with the Flierl (1987) estimate of the Gulf Stream's nondimensional beta between 0.02 and 0.13.

## REFERENCES


Adams, J. P., P. Swarztrauber, and R. Sweet, 1988: FISHPAK: Efficient FORTRAN subprograms for the solution of separable elliptic partial differential equations. NCAR, https://www2.cisl.ucar.edu/resources/legacy/fishpack.

Arakawa, A., 1966: Computational design for long-term numerical integration of the equations of fluid motion: Two-dimensional incompressible flow. Part I. *J. Comput. Phys.*, **1**, 119–143, https://doi.org/10.1016/0021-9991(66)90015-5.

Beliakova, N. Y., 1999: Generation and maintenance of recirculation by Gulf Stream instabilities. Ph.D. dissertation, Massachusetts Institute of Technology–Woods Hole Oceanographic Institution Joint Program, 224 pp., http://hdl.handle.net/1721.1/58539.

Berloff, P., A. M. Hogg, and W. Dewar, 2007: The turbulent oscillator: A mechanism of low-frequency variability of the wind-driven ocean gyres. *J. Phys. Oceanogr.*, **37**, 2363–2386, https://doi.org/10.1175/JPO3118.1.

Bower, A. S., and N. G. Hogg, 1992: Evidence for barotropic wave radiation for the Gulf Stream. *J. Phys. Oceanogr.*, **22**, 42–61, https://doi.org/10.1175/1520-0485(1992)022<0042:EFBWRF>2.0.CO;2.

——, and ——, 1996: Structure of the Gulf Stream and its recirculations at 55°W. *J. Phys. Oceanogr.*, **26**, 1002–1022, https://doi.org/10.1175/1520-0485(1996)026<1002:SOTGSA>2.0.CO;2.

——, H. T. Rossby, and J. L. Lillibridge, 1985: The Gulf Stream—Barrier or blender? *J. Phys. Oceanogr.*, **15**, 24–32, https://doi.org/10.1175/1520-0485(1985)015<0024:TGSOB>2.0.CO;2.

——, M. S. Lozier, S. F. Gary, and C. W. Böning, 2009: Interior pathways of the North Atlantic meridional overturning circulation. *Nature*, **459**, 243–247, https://doi.org/10.1038/nature07979.

——, ——, and ——, 2011: Export of Labrador Sea Water from the subpolar North Atlantic: A Lagrangian perspective. *Deep-Sea Res. II*, **58**, 1798–1818, https://doi.org/10.1016/j.dsr2.2010.10.060.

Buckley, M. W., and J. Marshall, 2015: Observations, inferences, and mechanisms of the Atlantic Meridional Overturning Circulation: A review. *Rev. Geophys.*, **54**, 5–63, https://doi.org/10.1002/2015RG000493.

Cessi, P., 1988: A stratified model of the inertial recirculation. *J. Phys. Oceanogr.*, **18**, 662–682, https://doi.org/10.1175/1520-0485(1988)018<0662:ASMOTI>2.0.CO;2.

——, 1990: Recirculation and separation of boundary currents. *J. Mar. Res.*, **48**, 1–35, https://doi.org/10.1357/002224090784984597.

——, G. Ierley, and W. Young, 1987: A model of the inertial recirculation driven by potential vorticity anomalies. *J. Phys. Oceanogr.*, **17**, 1640–1652, https://doi.org/10.1175/1520-0485(1987)017<1640:AMOTIR>2.0.CO;2.

Cherian, D. A., and K. H. Brink, 2016: Offshore transport of shelf water by deep-ocean eddies. *J. Phys. Oceanogr.*, **46**, 3599–3621, https://doi.org/10.1175/JPO-D-16-0085.1.

Dewar, W. K., 1998: Topography and barotropic transport control by bottom friction. *J. Mar. Res.*, **56**, 295–328, https://doi.org/10.1357/002224098321822320.

Durran, D. R., 1991: The third-order Adams–Bashforth method: An attractive alternative to leapfrog time differencing. *Mon. Wea. Rev.*, **119**, 702–720, https://doi.org/10.1175/1520-0493(1991)119<0702:TTOABM>2.0.CO;2.

Flierl, G., 1987: Isolated eddy models in geophysics. *Annu. Rev. Fluid Mech.*, **19**, 493–530, https://doi.org/10.1146/annurev.fl.19.010187.002425.

Fofonoff, N., 1954: Steady flow in a frictionless homogeneous ocean. *J. Mar. Res.*, **13**, 254–262.

Gary, S. F., M. S. Lozier, W. B. Claus, and A. Biastoch, 2011: Deciphering the pathways for the deep limb of the meridional overturning circulation. *Deep-Sea Res. II*, **58**, 1781–1797, https://doi.org/10.1016/j.dsr2.2010.10.059.

Greatbatch, R. J., 1987: A model for the inertial recirculation of a gyre. *J. Mar. Res.*, **45**, 601–634, https://doi.org/10.1357/002224087788326821.

Haidvogel, D. B., and P. B. Rhines, 1983: Waves and circulation driven by oscillatory winds in an idealized ocean basin. *Geophys. Astrophys. Fluid Dyn.*, **25**, 1–63, https://doi.org/10.1080/03091928308221747.

Hogg, N. G., 1983: A note on the deep circulation of the western North Atlantic: Its nature and causes. *Deep-Sea Res.*, **30A**, 945–961, https://doi.org/10.1016/0198-0149(83)90050-X.

——, 1992: On the transport of the Gulf Stream between Cape Hatteras and the Grand Banks. *Deep-Sea Res.*, **39**, 1231–1246, https://doi.org/10.1016/0198-0149(92)90066-3.

——, 2000: Low-frequency variability on the western flanks of the Grand Banks. *J. Mar. Res.*, **58**, 523–545, https://doi.org/10.1357/002224000321511007.

——, and H. Stommel, 1985: On the relation between the deep circulation and the Gulf Stream. *Deep-Sea Res.*, **32A**, 1181–1193, https://doi.org/10.1016/0198-0149(85)90002-0.

——, R. S. Pickart, R. M. Hendry, and W. J. Smethie, 1986: The northern recirculation gyre of the Gulf Stream. *Deep-Sea Res.*, **33A**, 1139–1165, https://doi.org/10.1016/0198-0149(86)90017-8.

Holland, W. R., and P. B. Rhines, 1980: An example of eddy-induced ocean circulation. *J. Phys. Oceanogr.*, **10**, 1010–1031, https://doi.org/10.1175/1520-0485(1980)010<1010:AEOEIO>2.0.CO;2.

Jayne, S. R., and N. G. Hogg, 1999: On recirculation forced by an unstable jet. *J. Phys. Oceanogr.*, **29**, 2711–2718, https://doi.org/10.1175/1520-0485(1999)029<2711:ORFBAU>2.0.CO;2.

——, ——, and P. Malanotte-Rizzoli, 1996: Recirculation gyres forced by a beta-plane jet. *J. Phys. Oceanogr.*, **26**, 492–504, https://doi.org/10.1175/1520-0485(1996)026<0492:RGFBAB>2.0.CO;2.

Knauss, J. A., 1969: A note on the transport of the Gulf Stream. *Deep-Sea Res.*, **16** (Suppl.), 117–123.

Kondrashov, D., and P. Berloff, 2015: Stochastic modeling of decadal variability in ocean gyres. *Geophys. Res. Lett.*, **42**, 1543–1553, https://doi.org/10.1002/2014GL062871.

Le Bras, I. A., 2017: Dynamics of North Atlantic western boundary currents. Ph.D. dissertation, Massachusetts Institute of Technology–Woods Hole Oceanographic Institution Joint Program, 174 pp., https://doi.org/10.1575/1912/8657.

——, I. Yashayaev, and J. M. Toole, 2017: Tracking Labrador Sea Water property signals along the Deep Western Boundary Current. *J. Geophys. Res. Oceans*, **122**, 5348–5366, https://doi.org/10.1002/2017JC012921.

Leaman, K., E. Johns, and T. Rossby, 1989: The average distribution of volume transport and potential vorticity with temperature at three sections across the Gulf Stream. *J. Phys. Oceanogr.*, **19**, 36–51, https://doi.org/10.1175/1520-0485(1989)019<0036:TADOVT>2.0.CO;2.

Lozier, M. S., 1997: Evidence for large-scale eddy-driven gyres in the North Atlantic. *Science*, **277**, 361–364, https://doi.org/10.1126/science.277.5324.361.

——, S. F. Gary, and A. S. Bower, 2013: Simulated pathways of the overflow waters in the North Atlantic: Subpolar to subtropical export. *Deep-Sea Res. II*, **85**, 147–153, https://doi.org/10.1016/j.dsr2.2012.07.037.

Malanotte-Rizzoli, P., N. G. Hogg, and R. E. Young, 1995: Stochastic wave radiation by the Gulf Stream: Numerical experiments. *Deep-Sea Res. I*, **42**, 389–423, https://doi.org/10.1016/0967-0637(95)00001-M.

Marshall, J., and G. Nurser, 1986: Steady, free circulation in a stratified quasi-geostrophic ocean. *J. Phys. Oceanogr.*, **16**, 1799–1813, https://doi.org/10.1175/1520-0485(1986)016<1799:SFCIAS>2.0.CO;2.

McDowell, S., P. Rhines, and T. Keffer, 1982: North Atlantic potential vorticity and its relation to the general circulation. *J. Phys. Oceanogr.*, **12**, 1417–1435, https://doi.org/10.1175/1520-0485(1982)012<1417:NAPVAI>2.0.CO;2.

Meinen, C. S., and D. S. Luther, 2016: Structure, transport, and vertical coherence of the Gulf Stream from the Straits of Florida to the southeast Newfoundland Ridge. *Deep-Sea Res. I*, **112**, 137–154, https://doi.org/10.1016/j.dsr.2016.03.002.

Mertens, C., M. Rhein, M. Walter, C. W. Boning, E. Behrens, D. Kieke, R. Steinfeldt, and U. Stober, 2014: Circulation and transports in the Newfoundland Basin, western subpolar North Atlantic. *J. Geophys. Res. Oceans*, **119**, 7772–7793, https://doi.org/10.1002/2014JC010019.

Mizuta, G., 2009: Rossby wave radiation from an eastward jet and its recirculations. *J. Mar. Res.*, **67**, 185–212, https://doi.org/10.1357/002224009789051227.

Pickart, R. S., and W. M. J. Smethie, 1993: How does the Deep Western Boundary Current cross the Gulf Stream? *J. Phys. Oceanogr.*, **23**, 2602–2616, https://doi.org/10.1175/1520-0485(1993)023<2602:HDTDWB>2.0.CO;2.

——, N. G. Hogg, and W. M. Smethie, 1989: Determining the strength of the Deep Western Boundary Current using the chlorofluoromethane ratio. *J. Phys. Oceanogr.*, **19**, 940–951, https://doi.org/10.1175/1520-0485(1989)019<0940:DTSOTD>2.0.CO;2.

Rhines, P. B., and W. R. Holland, 1979: A theoretical discussion of eddy-driven mean flows. *Dyn. Atmos. Oceans*, **3**, 289–325, https://doi.org/10.1016/0377-0265(79)90015-0.

——, and W. R. Young, 1982: Homogenization of potential vorticity in planetary gyres. *J. Fluid Mech.*, **122**, 347–367, https://doi.org/10.1017/S0022112082002250.

Richardson, P. L., 1985: Average velocity and transport of the Gulf Stream near 55W. *J. Mar. Res.*, **43**, 83–111, https://doi.org/10.1357/002224085788437343.

Riviere, P., A. M. Treguier, and P. Klein, 2004: Effects of bottom friction on nonlinear equilibration of an oceanic baroclinic jet. *J. Phys. Oceanogr.*, **34**, 416–432, https://doi.org/10.1175/1520-0485(2004)034<0416:EOBFON>2.0.CO;2.

Schott, F. A., J. Fischer, M. Dengler, and R. Zantopp, 2006: Variability of the Deep Western Boundary Current east of the Grand Banks. *Geophys. Res. Lett.*, **33**, L21S07, https://doi.org/10.1029/2006GL026563.

Spall, M. A., 1996: Dynamics of the Gulf Stream/Deep Western Boundary Current crossover. Part 1: Entrainment and recirculation. *J. Phys. Oceanogr.*, **26**, 2152–2168, https://doi.org/10.1175/1520-0485(1996)026<2152:DOTGSW>2.0.CO;2.

Talley, L. D., and M. S. McCartney, 1982: Distribution and circulation of Labrador Sea Water. *J. Phys. Oceanogr.*, **12**, 1189–1205, https://doi.org/10.1175/1520-0485(1982)012<1189:DACOLS>2.0.CO;2.

Toole, J. M., R. G. Curry, T. M. Joyce, M. McCartney, and B. Peña-Molino, 2011: Transport of the North Atlantic Deep Western Boundary Current about 39°N, 70°W: 2004–2008. *Deep-Sea Res. II*, **58**, 1768–1780, https://doi.org/10.1016/j.dsr2.2010.10.058.

——, M. Andres, I. A. Le Bras, T. M. Joyce, and M. S. McCartney, 2017: Moored observations of the Deep Western Boundary Current in the NW Atlantic: 2004–2014. *J. Geophys. Res. Oceans*, **122**, 7488–7505, https://doi.org/10.1002/2017JC012984.

Venaille, A., G. K. Vallis, and K. Shafer Smith, 2011: Baroclinic turbulence in the ocean: Analysis with primitive equation and quasigeostrophic simulations. *J. Phys. Oceanogr.*, **41**, 1605–1623, https://doi.org/10.1175/JPO-D-10-05021.1.

Waterman, S., and S. R. Jayne, 2011: Eddy-mean flow interactions in the along-stream development of a western boundary current jet: An idealized model study. *J. Phys. Oceanogr.*, **41**, 682–707, https://doi.org/10.1175/2010JPO4477.1.

——, and ——, 2012: Eddy-driven recirculations from a localized transient forcing. *J. Phys. Oceanogr.*, **42**, 430–447, https://doi.org/10.1175/JPO-D-11-060.1.

——, N. G. Hogg, and S. R. Jayne, 2011: Eddy-mean flow interaction in the Kuroshio extension region. *J. Phys. Oceanogr.*, **41**, 1182–1208, https://doi.org/10.1175/2010JPO4564.1.

Worthington, L. V., 1976: *On the North Atlantic Circulation*. Johns Hopkins Oceanographic Studies, Vol. 6, Johns Hopkins University Press, 110 pp.

Wunsch, C., 2005: The total meridional heat flux and its oceanic and atmospheric partition. *J. Climate*, **18**, 4374–4380, https://doi.org/10.1175/JCLI3539.1.

Xu, X., P. B. Rhines, E. P. Chassignet, and W. J. Schmitz, 2015: Spreading of Denmark Strait overflow water in the western subpolar North Atlantic: Insights from eddy-resolving simulations with a passive tracer. *J. Phys. Oceanogr.*, **45**, 2913–2932, https://doi.org/10.1175/JPO-D-14-0179.1.

Zantopp, R., J. Fischer, M. Visbeck, and J. Karstensen, 2017: From interannual to decadal: 17 years of boundary current transports at the exit of the Labrador Sea. *J. Geophys. Res. Oceans*, **122**, 1724–1748, https://doi.org/10.1002/2016JC012271.

Zhang, R., and G. K. Vallis, 2007: The role of bottom vortex stretching on the path of the North Atlantic western boundary current and on the northern recirculation gyre. *J. Phys. Oceanogr.*, **37**, 2053–2080, https://doi.org/10.1175/JPO3102.1.